

An Optimized Correction Procedure via Reconstruction Formulation for Broadband Wave Computation

Yi Li* and Z. J. Wang

Department of Aerospace Engineering and CFD Center, Iowa State University, Ames, IA 50011, USA.

Received 30 July 2011; Accepted (in revised version) 7 May 2012

Available online 8 October 2012

Abstract. Recently, a new differential discontinuous formulation for conservation laws named the Correction Procedure via Reconstruction (CPR) is developed, which is inspired by several other discontinuous methods such as the discontinuous Galerkin (DG), the spectral volume (SV)/spectral difference (SD) methods. All of them can be unified under the CPR formulation, which is relatively simple to implement due to its finite-difference-like framework. In this paper, a different discontinuous solution space including both polynomial and Fourier basis functions on each element is employed to compute broad-band waves. Free-parameters introduced in the Fourier bases are optimized to minimize both dispersion and dissipation errors through a wave propagation analysis. The optimization procedure is verified with a mesh resolution analysis. Numerical results are presented to demonstrate the performance of the optimized CPR formulation.

AMS subject classifications: 76

Key words: CPR (correction procedure via reconstruction), hybrid discontinuous space, wave propagation analysis, unstructured meshes.

1 Introduction

In the last two decades, there has been a surge of research activities on high-order methods capable of solving the Navier-Stokes equations on unstructured grids. For a review of some of these activities, the readers can refer to [11, 44]. Many powerful high-order numerical algorithms have been developed, e.g. the spectral element method [30], multi-domain spectral method [20, 21], k-exact finite volume method [4], WENO methods [14], discontinuous Galerkin (DG) method [5, 8, 9], high-order residual distribution

*Corresponding author. *Email addresses:* yili@iastate.edu (Y. Li), zjw@iastate.edu (Z. J. Wang)

methods [1], spectral volume (SV) [27, 33, 43, 48, 49] and spectral difference (SD) methods [16, 26, 29, 34, 35, 50, 51]. A new discontinuous formulation named Correction Procedure via Reconstruction (CPR) was recently developed in [17], and extended to simplex meshes in [46]. The degrees-of-freedom (DOFs) are the state variables at solution points (SPs) in the CPR formulation, where the differential form of the governing equation is solved. As a result, explicit surface and volume integrals are avoided. The CPR formulation is among the most efficient discontinuous methods in terms of the number of operations.

The stability and accuracy of the discontinuous high-order methods depend on how the solutions are approximated and the weighting functions are chosen. The piecewise polynomial space is commonly chosen for convection problems. However, piecewise polynomials may not provide the best approximation for some PDEs and initial/boundary conditions. We now list some examples in the literature. The locally divergence-free polynomial space was used in the DG method to solve the Maxwell equations and better results were achieved compared to the classical piecewise polynomial space in [7, 22–24]. Exponential functions were proposed to solve singular perturbation problems by Kadalbajoo and Patidar [19] and by Reddy and Chakravarthy [31]. Non-polynomial spaces were used in the local essentially non-oscillatory (ENO) reconstruction for solving hyperbolic conservation laws in [6]. Another work is the use of exponential functions near a boundary, and the use of trigonometric functions for highly oscillatory problems, as shown by Yuan and Shu [52].

In the present study, a hybrid space including both polynomial and Fourier functions are employed to resolve broadband wave propagation problems. Fourier functions are used such that the method can exactly represent waves at certain wave numbers, while polynomial functions are employed to preserve a certain order of accuracy. Free-parameters introduced in the Fourier functions are optimized by mimicking the dispersion-relation-preserving (DRP) method to minimize both dispersion and dissipation errors [25, 32, 36, 37, 54, 55]. The basic idea of the DRP method is to optimize the scheme coefficients for the high resolution of short waves with respect to the computation grid instead of the truncation errors. The present method is named a frequency optimized CPR formulation (FOCPR) in the present paper.

Fourier analyses have been preformed to investigate the dispersive and dissipative errors for finite difference and finite volume methods [25, 32, 36, 37, 54, 55]. Hu [15] applied it for the DG method, and Van den Abeele et al. [42] carried out such an analysis for the 1D spectral volume method. In this paper, the accuracy and stability properties of the CPR method with the hybrid spaces are assessed by following similar techniques. A mesh resolution analysis is also performed to study the points-per-wavelength (PPW) requirement to achieve a certain accuracy following the procedure in [18, 53] in order to verify the optimization procedure. Several numerical tests are performed, which show that the FOCPR method can resolve broadband waves more accurately than the original CPR method.

This paper is organized as follows. For the sake of completeness, the framework

of the CPR method is given in Section 2. In Section 3, free-parameters introduced in the Fourier bases are optimized by minimizing the integral dispersion and dissipation errors. In addition, a mesh resolution analysis is carried out to verify the optimization procedure. In Section 4, a two-dimensional wave propagation analysis is conducted for quadrilateral grids with a tensor product basis. In Section 5, numerical tests are presented to demonstrate the performance of the FOCPR method. Concluding remarks are given in Section 6.

2 Review of the CPR method

The CPR formulation can be derived from a weighted residual method by transforming the integral formulation into a differential one. The hyperbolic conservation law can be written as

$$\frac{\partial u}{\partial t} + \nabla \cdot \vec{F}(u) = 0, \tag{2.1}$$

with proper initial and boundary conditions, where u is the state vector, and \vec{F} is the flux vector. The computation domain Ω is discretized into N non-overlapping triangular elements $\{V_i\}_{i=1}^N$. Let W be an arbitrary weighting function or test function. Multiplying Eq. (2.1) with an arbitrary weighting function W and integrating over an element V_i , we obtain

$$\int_{V_i} \left(\frac{\partial u}{\partial t} + \nabla \cdot \vec{F}(u) \right) W dV = \int_{V_i} \frac{\partial u}{\partial t} W dV + \int_{\partial V_i} W \vec{F}(u) \cdot \vec{n} ds - \int_{V_i} \nabla W \cdot \vec{F}(u) dV = 0. \tag{2.2}$$

Let u_i be an approximate solution to the analytical solution u on element V_i . The global solution is discontinuous across element interfaces. On each element, we assume that the solution belongs to the space of polynomials of degree k or less, i.e., $u_i \in P^k(V_i)$, (or P^k if there is no confusion). Let the dimension of P^k be $K = (k+1)(k+2)/2$. In addition, the numerical solution u_i is required to satisfy Eq. (2.2)

$$\int_{V_i} \frac{\partial u_i}{\partial t} W dV + \int_{\partial V_i} W \vec{F}(u_i) \cdot \vec{n} ds - \int_{V_i} \nabla W \cdot \vec{F}(u_i) dV = 0. \tag{2.3}$$

The surface integral is not properly defined because the numerical solution is discontinuous across element interfaces. Following the idea used in the Godunov method, the normal flux term in Eq. (2.3) is replaced with a common Riemann flux, e.g.,

$$F^n(u_i) \equiv \vec{F}(u_i) \cdot \vec{n} \approx F_{com}^n(u_i, u_{i+}, \vec{n}), \tag{2.4}$$

where u_{i+} denotes the solution outside the current element V_i . Instead of Eq. (2.3), the approximate solution is required to satisfy

$$\int_{V_i} \frac{\partial u_i}{\partial t} W dV + \int_{\partial V_i} W F_{com}^n(u_i, u_{i+}, \vec{n}) ds - \int_{V_i} \nabla W \cdot \vec{F}(u_i) dV = 0. \tag{2.5}$$

Applying integration by parts again to the last term of the above LHS, we obtain

$$\int_{V_i} \frac{\partial u_i}{\partial t} W dV + \int_{V_i} W \nabla \cdot \vec{F}(u_i) dV + \int_{\partial V_i} W [F_{com}^n(u_i, u_{i+}, \vec{n}) - F^n(u_i)] dS = 0. \quad (2.6)$$

Here, the test space has the same dimension as the solution space, and is chosen in a manner to guarantee the existence and uniqueness of the numerical solution.

Note that the quantity $\nabla \cdot \vec{F}(u_i)$ involves no influence from the data in the neighboring cells. The influence of these data is represented by the above boundary integral, which is also called a "penalty term", penalizing the normal flux differences.

The next step is critical in the elimination of the test function. The boundary integral above is cast as a volume integral via the introduction of a "correction field" on V_i , $\delta_i \in P^k(V_i)$,

$$\int_{V_i} W \delta_i dV = \int_{\partial V_i} W [F^n] dS, \quad (2.7)$$

where $[F^n] = F_{com}^n(u_i, u_{i+}, \vec{n}) - F^n(u_i)$ is the normal flux difference. The above equation is sometimes referred to as the "lifting operator", which has the normal flux differences on the boundary as input and a member of $P^k(V_i)$ as output. Substituting Eq. (2.7) into Eq. (2.6), we obtain

$$\int_{V_i} \left[\frac{\partial u_i}{\partial t} + \nabla \cdot \vec{F}(u_i) + \delta_i \right] W dV = 0. \quad (2.8)$$

If the flux vector is a linear function of the state variable, then $\nabla \cdot \vec{F}(u_i) \in P^k$. In this case, the terms inside the square bracket are all elements of P^k . Because the test space is selected to ensure a unique solution, Eq. (2.8) is equivalent to

$$\frac{\partial u_i}{\partial t} + \nabla \cdot \vec{F}(u_i) + \delta_i = 0. \quad (2.9)$$

For nonlinear conservation laws, $\nabla \cdot \vec{F}(u_i)$ is usually not an element of P^k . As a result, Eq. (2.8) cannot be reduced to Eq. (2.9). In this case, the most obviously choice is to project $\nabla \cdot \vec{F}(u_i)$ into P^k . Denote $\Pi(\nabla \cdot \vec{F}(u_i))$ a projection of $\nabla \cdot \vec{F}(u_i)$ to P^k . Once choice is

$$\int_{V_i} \Pi(\nabla \cdot \vec{F}(u_i)) W dV = \int_{V_i} \nabla \cdot \vec{F}(u_i) W dV. \quad (2.10)$$

Then Eq. (2.8) reduces to

$$\frac{\partial u_i}{\partial t} + \Pi(\nabla \cdot \vec{F}(u_i)) + \delta_i = 0. \quad (2.11)$$

With the introduction of the correction field δ_i , and a projection of $\Pi(\nabla \cdot \vec{F}(u_i))$ for nonlinear conservation laws, we have reduced the weighted residual formulation to a different formulation, which involves no explicit integrals. Note that for δ_i defined by Eq. (2.7), if $W \in P^k$, Eq. (2.11) is equivalent to the DG formulation, at least for linear conservation laws; if W belongs to another space, the resulting δ_i is different. We obtain a formulation corresponding to a different method such as the SV method.

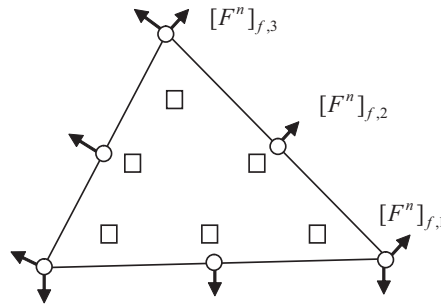


Figure 1: Solution points (squares) and flux points (circles) for a triangular element of $k=2$.

Next, let the DOFs be the solutions at a set of solution points (SPs) $\{\vec{r}_{ij}\}$ (j varies from 1 to K), as shown in Fig. 1. Then Eq. (2.11) holds true at the SPs, i.e.,

$$\frac{\partial u_{i,j}}{\partial t} + \Pi_j(\nabla \cdot \vec{F}(u_i)) + \delta_{i,j} = 0, \tag{2.12}$$

where $\Pi_j(\nabla \cdot \vec{F}(u_i))$ denotes the values of $\Pi(\nabla \cdot \vec{F}(u_i))$ at SP j . The efficiency of the CPR approach hinges on how the correction field δ_i and the projection $\Pi(\nabla \cdot \vec{F}(u_i))$ are computed. To compute δ_i , we define $k+1$ points named flux points (FPs) along each interface, where the normal flux differences $[F^n]$ are computed, as shown in Fig. 1. We approximate (for nonlinear conservation laws) the normal flux difference $[F^n]$ with a degree k interpolation polynomial along each interface,

$$[F^n]_f \approx I_k[F^n]_f \equiv \sum_l [F^n]_{f,l} L_l^{FP}, \tag{2.13}$$

where f is an face (or edge in 2D) index, and l is the FP index, and L_l^{FP} is the Lagrange interpolation polynomial based on the FPs in a local interface coordinate. For linear triangles with straight edges, once the solutions points and flux points are chosen, the correction at the SPs can be written as

$$\delta_{i,j} = \frac{1}{|V_i|} \sum_{f \in \partial V_i} \sum_l \alpha_{j,f,l} [F^n]_{f,l} S_f, \tag{2.14}$$

where $\alpha_{j,f,l}$ are lifting constants independent of the solution, S_f is the face area, $|V_i|$ is the volume of V_i . Note that the correction for each solution point, namely $\delta_{i,j}$, is a linear combination of all the normal flux differences on all the faces of the cell. Conversely, a normal flux difference at a flux point on a face, say (f,l) results in a correction at a solution point j of an amount $\alpha_{j,f,l} [F^n]_{f,l} S_f / |V_i|$.

Substituting Eq. (2.14) into Eq. (2.12) we obtain the following CPR formulation

$$\frac{\partial u_{i,j}}{\partial t} + \Pi_j(\nabla \cdot \vec{F}(u_i)) + \frac{1}{|V_i|} \sum_{f \in \partial V_i} \sum_l \alpha_{j,f,l} [F^n]_{f,l} S_f = 0. \tag{2.15}$$

The 1D CPR formulation can be deduced from Eq. (??) as

$$\frac{\partial u_{i,j}}{\partial t} + \Pi_j \left(\frac{\partial F(u_i)}{\partial x} \right) + \frac{1}{|\Delta x_i|} (\alpha_{R,j} [F^n]_R + \alpha_{L,j} [F^n]_L) = 0, \quad (2.16)$$

where Δx_i is the length of element i , which has two interfaces, the left one and right one, with unit face areas and unit face normals of -1 and 1 respectively, $[F^n]_R$ and $[F^n]_L$ are the normal flux differences at the left and right interfaces, and $\alpha_{R,j}$ and $\alpha_{L,j}$ are the constant correction coefficients. It is often more convenient to transform the physical element in x to the standard element $[-1,1]$ with coordinate ξ resulting in the following transformed equation

$$\frac{\partial u}{\partial t} + \xi_x \frac{\partial F(u)}{\partial \xi} = 0. \quad (2.17)$$

The CPR formulation can be applied to (2.17) in a similar fashion.

3 Optimized CPR formulation with hybrid basis functions

Before we introduce the optimized CPR formulation, a Fourier analysis of the CPR method is performed to reveal its dispersive and dissipative characteristics. Then the basic idea for the optimized CPR method will be presented.

3.1 Fourier analysis of the CPR formulation

The scalar 1D wave equation is used as the model problem with a periodic boundary condition and a harmonic initial solution

$$\frac{\partial u}{\partial t} + a \frac{\partial u}{\partial x} = 0, \quad (3.1)$$

$$u(x,0) = e^{i\kappa x}, \quad (3.2)$$

where a is a positive wave speed, and K the wave number. A Fourier component of the form

$$u(x,t) = \hat{u} e^{I(\kappa x - \omega t) + \theta_R t}, \quad (3.3)$$

is considered as a solution of this linear advection equation, which represents a sinusoidal wave train with an angular frequency ω , and dissipation rate θ_R , where $I = \sqrt{-1}$. Eq. (3.3) is substituted into Eq. (3.1), and it is found that the exact dispersion relation is

$$\theta_R = 0 \quad \text{and} \quad \omega = a\kappa. \quad (3.4)$$

Non-dimensional quantities are introduced in this analysis. Suppose we employ a uniform mesh with mesh size Δx . The reference length scale is set as Δx and the time scale

is $\Delta x/a$. The dimensionless parameters are expressed as

$$Z = \kappa \Delta x, \tag{3.5}$$

$$\Omega = \omega \frac{\Delta x}{a}, \tag{3.6}$$

where Z and Ω are the non-dimensional wave number and frequency, respectively. The exact dispersion relation is then

$$\Omega = Z. \tag{3.7}$$

We can also substitute (3.3) into a numerical scheme, and obtain the numerical dispersion relation, which should be different from (3.7) and called the modified dispersion relation. This modified dispersion relation is close to the exact one. The difference is a measure of accuracy of the spatial discretization. The modified dissipation rate should be non-positive. Otherwise the solution will grow exponentially and the simulation becomes unstable.

We consider the standard element $\xi \in [-1, 1]$. The approximation solution can be written as

$$u_i = \sum_{j=1}^K W_j(\xi) u_{i,j}, \tag{3.8}$$

where $W_j(\xi)$ is the Lagrange polynomial. In 1D, $K = k + 1$. On the interface between two elements, say i and $i + 1$, a Riemann solver is used to compute the common flux

$$F_{Riemann}(u_i(1), u_{i+1}(-1)) = a \left(\frac{1+\beta}{2} u_i(1) + \frac{1-\beta}{2} u_{i+1}(-1) \right). \tag{3.9}$$

In Eq. (3.9), $\beta = 0$ corresponds to a central flux and $\beta = 1$ corresponds to the upwind flux. Upwind flux is employed in this paper. For the 1D scalar advection equation, the CPR scheme can be written in the following matrix form

$$\frac{du_{i,m}}{dt} + \sum_{j=1}^{k+1} N_{mj}^{-1} u_{i-1,j} + \sum_{j=1}^{k+1} N_{mj}^0 u_{i,j} = 0, \quad m = 1, \dots, k+1. \tag{3.10}$$

The matrices N^{-1} and N^0 are given in Appendix A. Substituting Eq. (3.3) into Eq. (3.10), we obtain the numerical dispersion relation for the CPR method

$$\det \left(-I\Omega + e^{-IZ} N^{-1} + N^0 \right) = 0. \tag{3.11}$$

Eq. (3.11) has $k + 1$ solutions, corresponding to the $k + 1$ eigenmodes of the numerical system. The quantity $-I\Omega$ is called the Fourier footprint \mathcal{R} . Let $\mathcal{R} = \mathcal{R}^{\text{Re}} + I\mathcal{R}^{\text{Im}}$, and the imaginary part \mathcal{R}^{Im} is a measure of dispersive properties of the scheme, whereas the real part \mathcal{R}^{Re} represents the diffusive behavior which should be non-positive for a stable scheme.

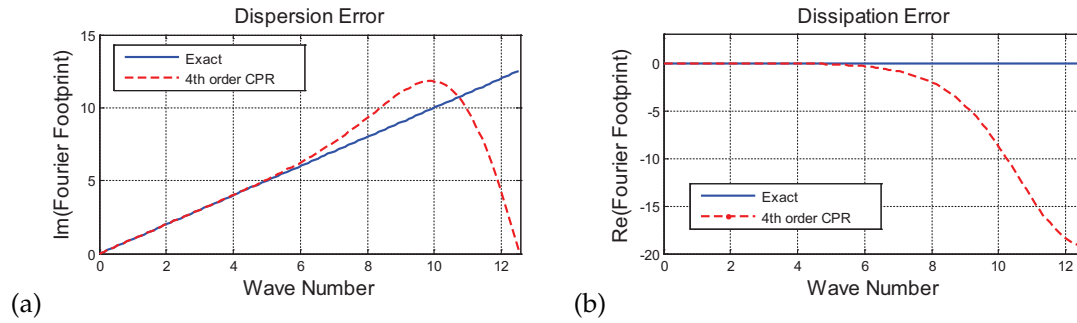


Figure 2: Diffusion and dissipation errors of the 4th order CPR schemes (\mathcal{R}^{Re} and \mathcal{R}^{Im} versus Z).

For a classic finite volume method, the wave number range is $-\pi < Z < \pi$, which corresponds to one degree of freedom (DOF) per element, while with a CPR scheme, the wave range is $-(k+1)\pi < Z < (k+1)\pi$, which is related to $k+1$ DOFs per element. To make a fair comparison between the finite volume and CPR schemes, the plot for the CPR method should be downscaled with a factor $k+1$ to take into account the higher number of DOFs per element.

In Fig. 2, the dispersive \mathcal{R}^{Im} and diffusive \mathcal{R}^{Re} properties are plotted versus the wave number for $k=3$ with a uniform solution point distribution. For this scheme, Z ranges from -4π to 4π . It is clear that the scheme is stable, because \mathcal{R}^{Re} is always non-positive. Note that the scheme becomes less accurate for increasing wave numbers. The present 4th order CPR scheme with a piece-wise polynomial basis has good wave propagation properties for dimensionless wave number up to $Z \approx 5$.

3.2 Frequency optimized CPR method

3.2.1 Basic idea

From Fig. 2(b), it is obviously that the higher the frequency, the more severely the waves are damped. Therefore higher frequency waves have more dissipative errors. In order to maximize the range of waves that can be resolved accurately, we need to reduce the error at higher frequency. The idea is to introduce Fourier components of certain frequencies ($\alpha_1, \alpha_2, \dots$) etc into the basis functions such that these frequencies can be resolved exactly. By properly choosing the frequencies, we try to resolve waves at the broadest range given a certain error threshold. For each element, we define the following three spaces: polynomial, Fourier and hybrid

$$B = \text{span}(1, x, x^2, x^3, \dots), \quad (3.12)$$

$$B = \text{span}(\sin(\alpha_1 * x), \cos(\alpha_1 * x), \sin(\alpha_2 * x), \cos(\alpha_2 * x), \dots), \quad (3.13)$$

$$B = \text{span}(1, x, x^2, x^3, \dots, \sin(\alpha_1 * x), \cos(\alpha_1 * x), \sin(\alpha_2 * x), \cos(\alpha_2 * x), \dots), \quad (3.14)$$

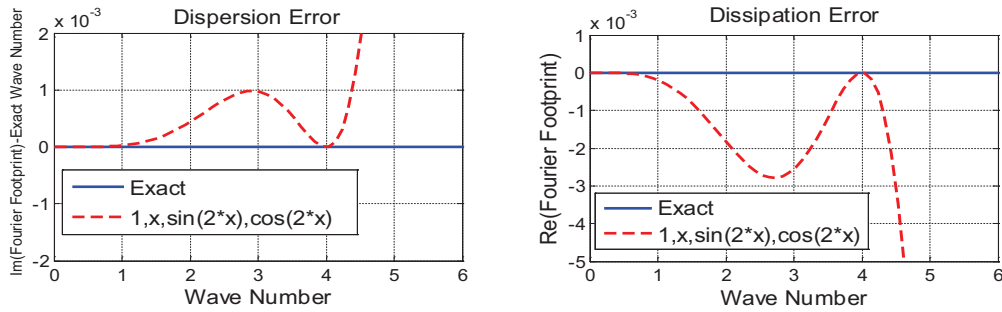


Figure 3: Dispersion error ($\mathcal{R}^{\text{Re}} - Z$) and dissipation error \mathcal{R}^{Im} versus Z for $B = (1, x, \sin(2*x), \cos(2*x))$.

where $(\alpha_1, \alpha_2, \dots)$ are free-parameters. The motivation to use the hybrid space instead of polynomial spaces is to obtain better approximation for broadband wave propagation, because a Fourier basis can exactly represent waves with certain wave numbers, while the polynomial basis is used in order to achieve a certain order accuracy with mesh refinement. The free-parameters are optimized to minimize both dispersion and dissipation errors over a specified range of wave numbers.

Due to the introduction of the Fourier component into the basis, the exact dispersion relation $\Omega = Z$ is exactly satisfied at a certain Z . In Fig. 3, both the dispersion ($\mathcal{R}^{\text{Re}} - Z$) and dissipation \mathcal{R}^{Im} errors are plotted with a hybrid basis $B = (1, x, \sin(2*x), \cos(2*x))$. It shows that dispersion and dissipation errors are equal to zero at the non-dimensional wave number 4 ($\Omega = Z = \kappa * \Delta x = 2 * 2 = 4$). Clearly the use of the hybrid basis reduces the errors at higher frequencies.

3.2.2 Dispersion-Relation-Preservation (DRP) Method

As stated in [36, 37], the wave propagation characteristics are encoded in the dispersion relation of the governing equations. The main idea of DRP schemes is to optimize high-order finite difference schemes not only to meet the usual conditions of consistency, stability and convergence, but also to have the same or almost the same dispersion relation as the original partial differential equations. The DRP methodology is reviewed here briefly.

The approximation of the first-order spatial derivative $\partial u / \partial x$ on a uniform grid for a finite difference scheme is given by

$$\left(\frac{\partial u}{\partial x}\right)_i \approx \frac{1}{\Delta x} \sum_{j=-L}^M a_j u(x_i + j\Delta x), \tag{3.15}$$

with M values to the right and L values to the left of the current point i . The finite difference scheme will be called the standard scheme if the coefficients a_j are determined from a Taylor series expansion. In the DRP scheme, the coefficients a_j are chosen by requiring the Fourier transform of the finite difference scheme on the right of Eq. (3.15)

to be a close approximation of the partial derivative on the left side. The finite difference Eq. (3.15) is a special case of the following equation in which x is a continuous variable:

$$\frac{\partial u}{\partial x}(x) \approx \frac{1}{\Delta x} \sum_{j=-L}^M a_j u(x+j\Delta x). \quad (3.16)$$

The Fourier transform and its inverse are related by

$$\tilde{u}(\alpha) = \frac{1}{2\pi} \int_{-\infty}^{\infty} u(x) e^{-I\alpha x} dx, \quad (3.17)$$

$$u(x) = \frac{1}{2\pi} \int_{-\infty}^{\infty} \tilde{u}(\alpha) e^{I\alpha x} d\alpha. \quad (3.18)$$

The Fourier transform of the both sides of Eq. (3.16) is

$$I\alpha \tilde{u} \approx \left(\frac{1}{\Delta x} \sum_{j=-L}^M a_j e^{I\alpha j\Delta x} \right) \tilde{u}, \quad (3.19)$$

or equivalently

$$\bar{\alpha} = \frac{-I}{\Delta x} \sum_{j=-L}^M a_j e^{I\alpha j\Delta x}. \quad (3.20)$$

The left side is the effective wave number and $\bar{\alpha}\Delta x$ is a function of $\alpha\Delta x$ with the period 2π . The coefficients a_j were chosen to minimize the integrated error E defined in Eq. (3.21) in order to assure that the Fourier transform of the finite difference scheme is a good approximation of the partial derivative over the range of wave numbers of interest

$$E = \int_{-\pi/2}^{\pi/2} |\alpha\Delta x - \bar{\alpha}\Delta x|^2 d(\alpha\Delta x) = \int_{-\pi/2}^{\pi/2} \left| IZ - \sum_{j=-L}^M a_j e^{IjZ} \right|^2 dZ. \quad (3.21)$$

The condition that E is a minimum are

$$\frac{\partial E}{\partial a_j} = 0, \quad j = -L, \dots, M. \quad (3.22)$$

Eq. (3.22) provides a system of linear algebraic equations by which the coefficients a_j can be determined.

3.2.3 Optimization of free-parameters of hybrid approximation space

Free-parameters in the hybrid basis for the CPR method are optimized by mimicking the idea of DRP to maximize the resolvable wave number range given a certain error threshold. The following two criteria are utilized.

The optimization process has to allow the normalized value of $\Omega_{\text{Im}}/K - Z/K$ and Ω_{Re}/K to be as close to zero as possible for certain integration wave numbers. K is the number of DOFs

$$E = \int_0^e |\Omega_{\text{Im}}/K - Z/K|^2 dZ + \lambda \int_0^e |\Omega_{\text{Re}}/K|^2 dZ. \tag{3.23}$$

The weight λ is set as 0.2 to balance the L_2 norm of the truncated dispersion and dissipation errors. e is a predetermined range of wave numbers.

In order to quantify the resolution of the scheme, we set the dispersion and dissipation errors to less than 0.5%, i.e. [52]

$$|\Omega_{\text{Im}} - Z| < 0.005 \quad \text{and} \quad |\Omega_{\text{Re}}| < 0.005. \tag{3.24}$$

In Table 1, the optimized parameters are displayed for the hybrid basis $(1, x, \sin(\alpha * x), \cos(\alpha * x))$. E -dispersion represents the integrated dispersion error, and E -dissipation represents the integrated dissipation error. Free-parameters α are found to minimize the integration error E for a certain wave number integration range e . In other words, the CPR schemes with shown in Table 1 have the minimum integration dispersion errors with respect to a given range e .

In Table 2, the maximum resolvable non-dimensional wave numbers Z_c are determined using Eq. (3.24) for each α with respect to a certain integration wave number e . This means when the non-dimensional wave numbers are smaller than Z_c , Eq. (3.24) is satisfied. In other words, when the non-dimensional wave number is greater than Z_c , the dispersion and dissipation errors are greater than 0.5%. So Z_c is called the maximum resolvable non-dimensional wave number. We can see that Z_c increases and then decreases as the integration range e increases. $\alpha = 2.1$ is referred as the optimized free-parameter, which minimizes the integration error E over a relatively large wave number integration

Table 1: Optimized free-parameter α of hybrid basis for $B = (1, x, \sin(\alpha * x), \cos(\alpha * x))$.

Integration range (e)	α	E -Dispersion	E -diffusion	E
$\pi \approx 3.14$	1.4	$2.1477e-09$	$2.7483e-08$	$7.6444e-09$
$5 * \pi / 4 \approx 3.93$	1.7	$1.6503e-07$	$1.0139e-06$	$3.6781e-07$
$3 * \pi / 2 \approx 4.71$	2.1	$3.8702e-06$	$2.4832e-05$	$8.8367e-06$
$7 * \pi / 4 \approx 5.50$	2.4	$6.1540e-05$	$2.6556e-04$	$1.1465e-04$
$2 * \pi \approx 6.28$	2.7	$6.5403e-04$	$2.1424e-03$	$1.0825e-03$

Table 2: Maximum resolvable wave number Z_c for a given error threshold $B = (1, x, \sin(\alpha * x), \cos(\alpha * x))$.

Integration range	α	Z_c
$\pi \approx 3.14$	1.4	3.9336
$5 * \pi / 4 \approx 3.93$	1.7	4.2336
$3 * \pi / 2 \approx 4.71$	2.1	4.8336
$7 * \pi / 4 \approx 5.50$	2.4	2.0336
$2 * \pi \approx 6.28$	2.7	1.6336

range 4.71, and at the same time the resolvable wave number Z_c reaches 4.83, with which both dispersion and dissipation errors are less than 0.5%. The same procedure is applied to schemes with more DOFs per element. For example, $\alpha = 4.0$ is the optimized free-parameter with the integration wave number range 8.60 for the base of $(1, x, x^2, x^3, \sin(\alpha * x), \cos(\alpha * x))$, and $\alpha_1 = 4.5$ and $\alpha_2 = 3.0$ are the optimized free-parameters with the integration wave number 9.42 for the base of $(1, x, \sin(\alpha_1 * x), \cos(\alpha_1 * x), \sin(\alpha_2 * x), \cos(\alpha_2 * x))$.

The upwind CPR schemes with the optimized hybrid space are compared with the corresponding polynomial spaces, Tam & Webb's central DRP and Zhuang & Chen upwind DRP in terms of dispersion and dissipation errors next.

In Fig. 4, the upwind CPR scheme with the optimized hybrid bases $B = (1, x, \sin(2.1 * x), \cos(2.1 * x))$ shows less dispersion errors than the polynomial basis and the Tam & Webb's central DRP scheme, but a little bit larger dispersion errors than Zhuang & Chen's upwind DRP scheme.

In Fig. 5, the optimized CPR scheme with 6 DOFs per element using hybrid basis $(1, x, x^2, x^3, \sin(4.0 * x), \cos(4.0 * x))$ has less dispersion errors than the corresponding CPR scheme with a polynomial bases, central DRP and upwind DRP schemes.

It also has less dissipation error than the upwind DPR scheme. Note that it is able to resolve waves with non-dimensional wave number as high as 1.6.

In Fig. 6, a FOCPR scheme with 2 Fourier components is compared with several other CPR schemes with 6 DOFs per element, and the two DPR schemes. The bases are also shown in these figures. The optimized CPR scheme with the hybrid basis $(1, x, \sin(3.0 * x), \cos(3.0 * x), \sin(4.5 * x), \cos(4.5 * x))$ has less dispersion and dissipation errors than the CPR scheme with one Fourier component $(1, x, x^2, x^3, \sin(4.0 * x), \cos(4.0 * x))$. It is able to resolve waves with a non-dimensional wave number as high as about 1.8. From the above analysis, it appears that more Fourier components in the hybrid basis result in a scheme with less dispersion and dissipation errors.

3.3 Mesh resolution analysis

In this section, the mesh resolution analysis is performed to verify the optimization procedure for the FOCPR method following the ideas in [18, 53]. The number of grid points-per-wavelength (PPW) is used as the main parameter to judge the performance of the various schemes in simulating wave propagation over long distances, e.g., for 200 wavelengths. In the following analysis, we employ the first order explicit Euler time discretization scheme with a very small time step so that the error is dominated by the spatial operator.

In one dimension, the error produced by the numerical scheme depends on the non-dimensional wave number Z and the courant number $C = a\Delta t / \Delta x$. In multi-dimensions, the error also depends on the wave direction relative to the grid. The mesh resolution analysis is based on the amplification factor $\omega(Z, C) = u^{m+1} / u^m$, where m is the time step index, and $\text{PPW} = \text{wavelength} / (\Delta x) = 2\pi / (K\Delta x)$.

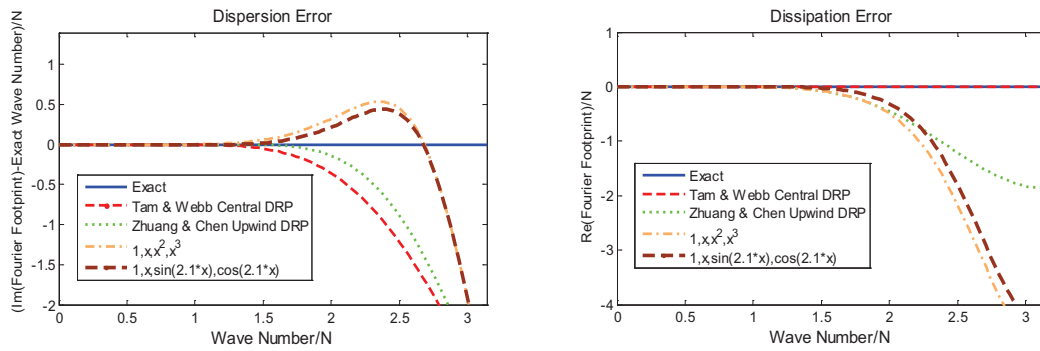


Figure 4: Comparison of normalized dispersion errors $(\mathcal{R}_{\text{Im}} - Z)/K$ and dissipation errors $\mathcal{R}_{\text{Re}}/K$ versus Z/K between DRP and CPR schemes with 4 DOFs per element.

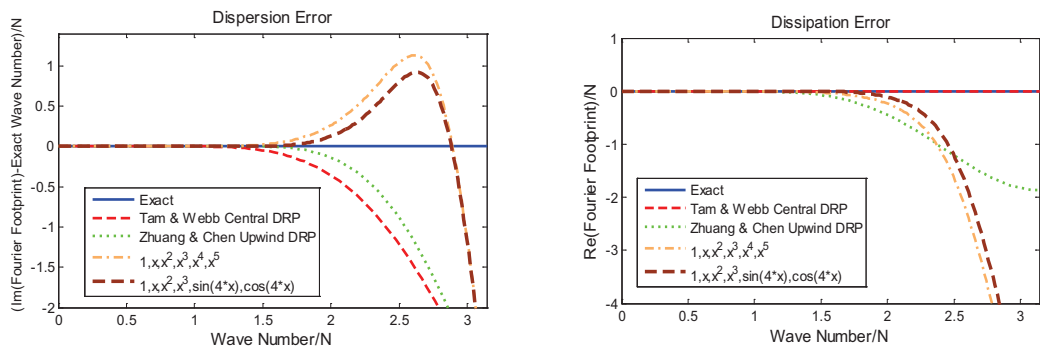


Figure 5: Comparison of normalized dispersion errors $(\mathcal{R}_{\text{Im}} - Z)/K$ and dissipation errors $\mathcal{R}_{\text{Re}}/K$ versus Z/K between DRP and CPR schemes with 6 DOFs per element.

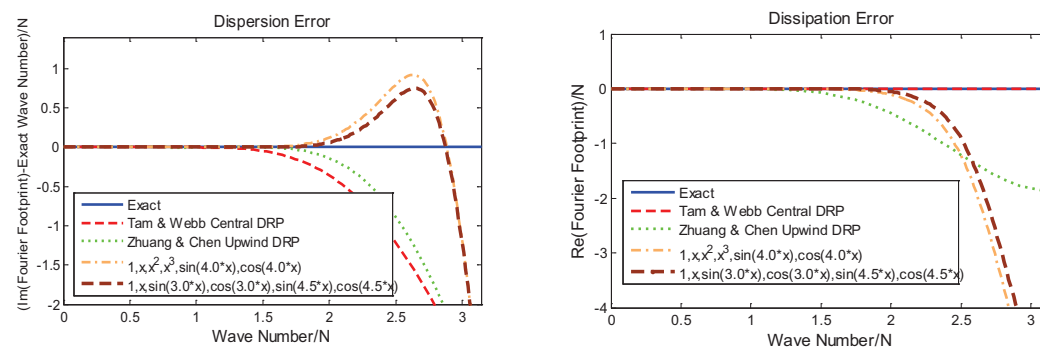


Figure 6: Comparison of normalized dispersion errors $(\mathcal{R}_{\text{Im}} - Z)/K$ and dissipation errors $\mathcal{R}_{\text{Re}}/K$ versus Z/K between DRP and CPR schemes with 6 DOFs with more Fourier components per element.

The local amplitude and phase errors are, respectively

$$Error_a = |\sigma| - 1, \quad (3.25)$$

$$Error_p = -\frac{\phi}{2C} - 1, \quad (3.26)$$

where $\phi = \tan^{-1}(\sigma_{\text{Im}}/\sigma_{\text{Re}})$, and σ_{Im} and σ_{Re} are the real and imaginary part of σ , respectively. The criterion for comparing schemes is based on the global amplitude and phase errors which are

$$Error_a = \left| |\sigma|^{\text{PPW} * n / C} - 1 \right| < 10\%, \quad (3.27)$$

$$Error_p = n * \left| \frac{\text{PPW} * \phi}{C} + 2\pi \right| < 10\%, \quad (3.28)$$

where n is the number of the wavelength travelled. In the following figures, the various methods are compared in terms of the PPW required to keep both the global amplitude and phase errors less than 10% as a function of the number of wavelength traveled. The dependence of the PPW requirements on the number of wavelengths is a reasonable measure for selecting a grid density and reveals the implication of the optimization.

In Fig. 7, the PPW requirements for FOCPR scheme with a hybrid basis of the form $(1, x, \sin(\alpha * x), \cos(\alpha * x))$ are presented. With $\alpha = 2$, the scheme performs well up to a distance of about 45 wavelengths based on a 10% global phase error criterion and about 15 wavelengths based on a 10% global amplitude error criterion and requires about less than 5.0 PPW. This behavior is typical of optimized schemes. Usually aggressive optimization leads to excellent performance for short distances of propagation but poor performance for longer distance. This property agrees with the previous analysis with the optimized free-parameter $\alpha = 2.1$, which is close to 2.

In Fig. 8, the PPW requirements for FOCPR schemes with a hybrid basis of the form $(1, x, x^2, x^3, \sin(\alpha * x), \cos(\alpha * x))$ are presented. With $\alpha = 4$, the scheme shows a typical behavior for optimized schemes. With this scheme at a resolution of 4.5 PPW, the waves can travel about 40 wavelengths with 10% phase error, and about 25 wavelengths with 10% amplitude error.

In Fig. 9, the PPW requirements for FOCPR schemes with a hybrid basis of the form $(1, x, \sin(\alpha_1 * x), \cos(\alpha_1 * x), \sin(\alpha_2 * x), \cos(\alpha_2 * x))$ are presented. With $\alpha_1 = 3.0$ and $\alpha_2 = 4.0$, the scheme shows the typical behavior too. The waves can travel 125 wavelengths with a resolution of 4.0 PPW, for 10% phase error, and 40 wavelengths with a resolution of 5.0 PPW for 10% amplitude error. The PPW analysis agrees well with the optimization analysis, and they can be used to verify each other.

4 Two-dimensional wave propagation analysis

The extension of the wave propagation analysis to 2D is described in this section. We consider the 2D linear advection equation and follow the ideas by Hu [15] and Van den

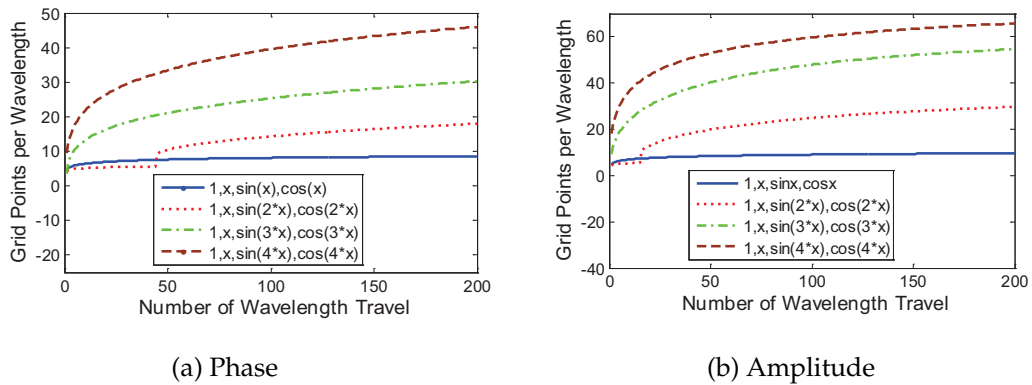


Figure 7: Grid resolution requirements based on the globe amplitude and phase errors for hybrid basis $(1, x, \sin(\alpha * x), \cos(\alpha * x))$.

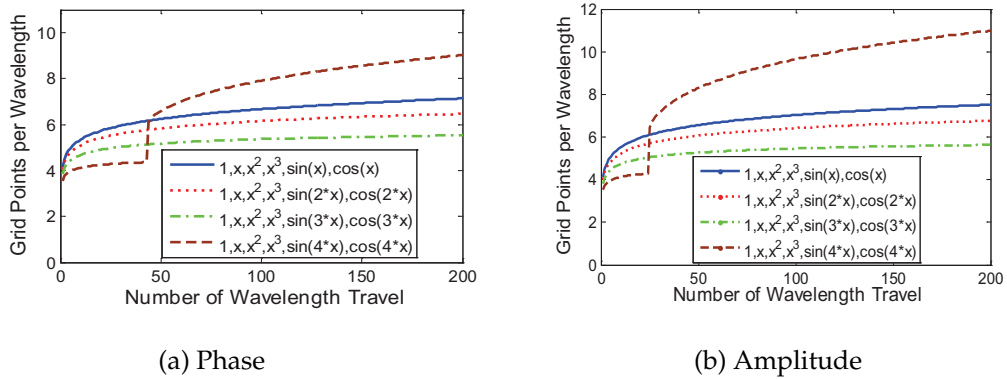


Figure 8: Grid resolution requirements based on globe amplitude and phase errors for hybrid basis $(1, x, x^2, x^4, \sin(\alpha * x), \cos(\alpha * x))$.

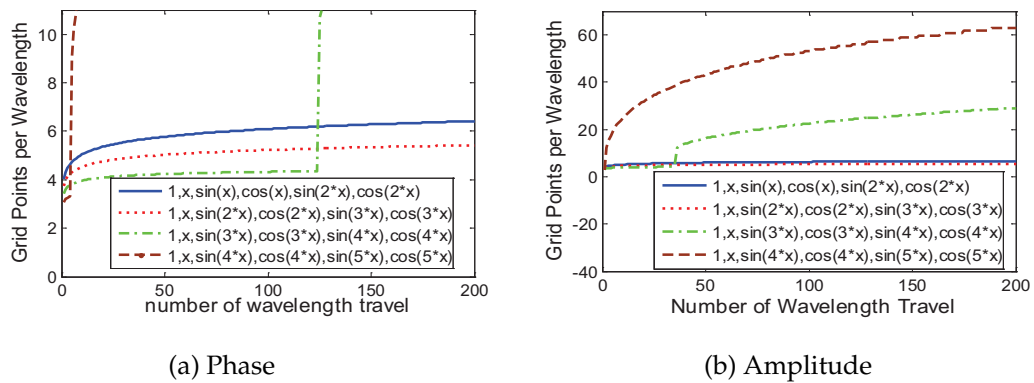


Figure 9: Grid resolution requirements based on globe amplitude and phase errors for hybrid basis $(1, x, \sin(\alpha 1 * x), \cos(\alpha 1 * x), \sin(\alpha 2 * x), \cos(\alpha 2 * x))$.

Abeele [39]

$$\frac{\partial u}{\partial t} + a_x \frac{\partial u}{\partial x} + a_y \frac{\partial u}{\partial y} = 0, \tag{4.1}$$

where $\vec{a} = [a_x \ a_y]^T = a\vec{l} = a[\cos\psi \ \sin\psi]^T$. The vector \vec{a} is the wave propagation velocity and is defined with the Cartesian components a_x and a_y , or defined with the amplitude a and the direction of the wave propagation ψ . A plane harmonic wave is given by

$$u(t, \vec{r}) = \hat{u}(t) * \exp\left(\vec{l} \cdot \vec{r} - I\omega t\right), \tag{4.2}$$

with $\vec{r} = [x \ y]^T$ and $\kappa = \kappa[\cos\theta \ \sin\theta]^T$, and θ is the orientation of the wave. Substituting Eq. (4.2) into Eq. (4.1), we obtain the following exact dispersion relation

$$\omega = a\kappa \cos(\psi - \theta). \tag{4.3}$$

The numerical dispersion relation corresponding to a discretization of the linear advection Eq. (4.1) with the CPR formulation is compared with the exact dispersion relation to study the dispersion and dissipation behavior. Similar to the 1D analysis, all quantities in this section are non-dimensional.

In the following analysis, we consider a uniform Cartesian grid with $\Delta_x = \Delta_y$, as shown in Fig. 10. The element is defined as $E^{n,m} = [x_n, x_{n+1}] \times [y_m, y_{m+1}]$ in Fig. 10(a). The DOFs on the standard element are shown in Fig. 10(b).

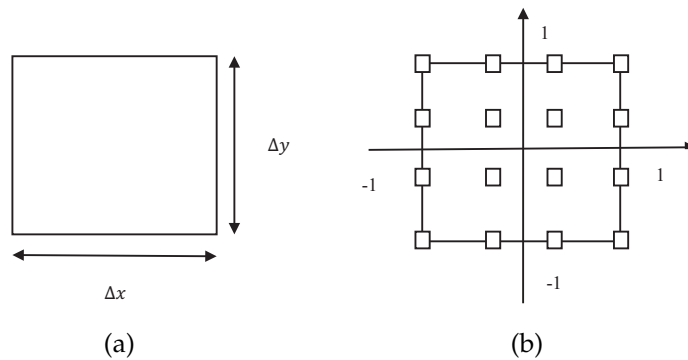


Figure 10: Rectangular mesh pattern and local coordinate system.

Similar to the 1D CPR formulation, the 2D CPR scheme for Eq. (4.1) can be written in the following form

$$\frac{\partial u^{n,m}}{\partial t} + a_x * \left[N^0 u^{n,m} + N^{-1} u^{n-1,m} \right] + a_y * \left[M^0 u^{n,m} + M^{-1} u^{n,m-1} \right] = 0. \tag{4.4}$$

Substituting (4.2) into (4.4), we obtain the numerical dispersion relation

$$\det \left(-I\tilde{\Omega} + \cos\psi \left(e^{-iZ\cos\theta} N^{-1} + N^0 \right) + \sin\psi \left(e^{-iZ\sin\theta} M^{-1} + M^0 \right) \right) = 0, \tag{4.5}$$

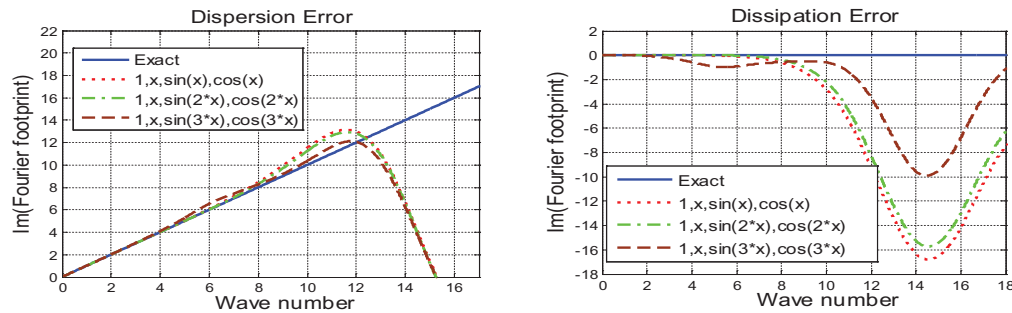


Figure 11: Dispersion and diffusion error as a function of the wave number for $\theta = \psi = \pi/6$.

where the matrices N^0 , N^{-1} , M^0 and M^{-1} are given in Appendix A. The determinant of the coefficient matrix must be zero for a non-trivial solution of u , which determines the dispersion relation for the semi-discretized equation. From Eq. (4.5) $\tilde{\Omega}$ should be found and compared to the non-dimensional exact frequency Ω , which is given by the exact dispersion relation $\Omega = Z \cos(\theta - \psi)$. Eq. (4.5) has $(k+1)^2$ solutions, corresponding to the eigenmodes of the numerical system. Similar to the one dimensional analysis, the quantity $-I\tilde{\Omega}$ is also called the Fourier footprint of the spatial discretization, whose imaginary part \mathcal{R}^{Im} is a measure of the dispersive properties of the scheme, whereas whose real part \mathcal{R}^{Re} reflects the diffusive behavior and should be non-positive for stable schemes for all Z , θ and ψ .

Fig. 11 shows the eigenvalues of Eq. (4.5) as a function of the wave number Z at $\theta = \psi = \pi/6$ for the FOCPR scheme with 4 DOFs in each direction. The choice of $\theta = \psi$ corresponds to a propagation direction parallel to the orientation of the plane wave. The exact dispersion relation is given by $\Omega = Z$ in this case. For this choice, the wavelength in the propagation direction is minimal, leading to the most severe test of the accuracy of the scheme. The wave propagation is anisotropic, especially for under-resolved waves. It can be concluded from the right figure of Fig. 11 that the scheme is stable for $\theta = \psi = \pi/6$, since \mathcal{R}^{Re} are always non-positive.

In Fig. 12, the phase speed ($\mathcal{R}^{\text{Re}}/Z$) is plotted as a function of angle ($\theta = \psi$) for $Z = \pi$, and it is obvious that the CPR scheme with a basis of $(1, x, \sin(x), \cos(x))$ produces less phase error than that with a basis of $(1, x, \sin(2x), \cos(2x))$, which in turn is more accurate than the scheme with the basis of $(1, x, \sin(3x), \cos(3x))$. In Fig. 13, the phase speed ($\mathcal{R}^{\text{Re}}/Z$) is plotted as a function of angle ($\theta = \psi$) for $Z = 1.5\pi$ and it is shown that the phase error of $(1, x, \sin(2x), \cos(2x)) <$ phase error of $(1, x, \sin(x), \cos(x)) <$ phase error of $(1, x, \sin(3x), \cos(3x))$. It is also obvious that the phase error for $Z = \pi$ is less than that for $Z = 1.5\pi$.

In Fig. 14, the dissipation rate (\mathcal{R}^{Im}) is plotted as a function of angle ($\theta = \psi$) for $Z = \pi$, and it is obvious that the amplitude error of $(1, x, \sin(x), \cos(x)) <$ amplitude error of $(1, x, \sin(2x), \cos(2x)) <$ amplitude error of $(1, x, \sin(3x), \cos(3x))$. In Fig. 15, the dissipation rate (\mathcal{R}^{Im}) is plotted as a function of angle ($\theta = \psi$) for $Z = 1.5\pi$ and it is

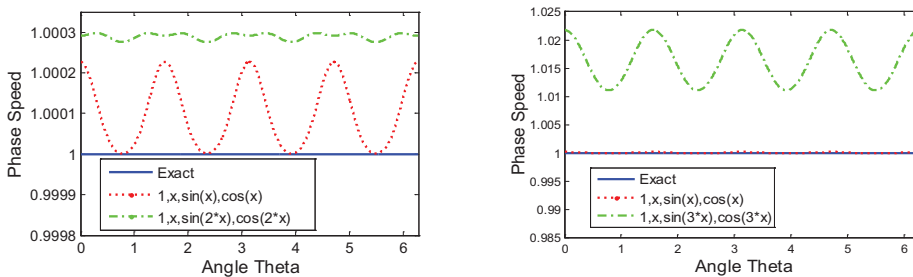


Figure 12: Phase speed ($\mathcal{R}^{\text{Re}}/K$) as function of $\theta (= \psi)$ for $Z = \pi$.

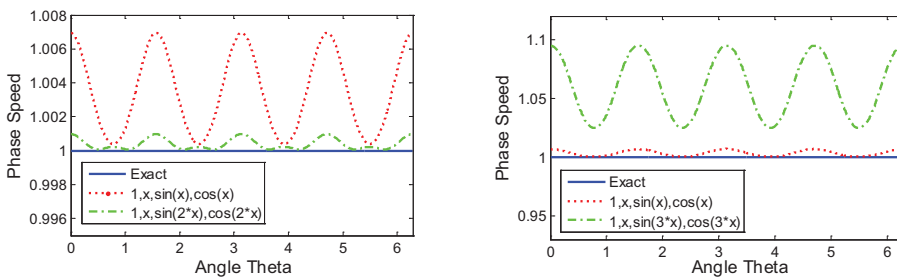


Figure 13: Phase speed ($\mathcal{R}^{\text{Re}}/K$) as function of $\theta (= \psi)$ for $Z = 1.5 * \pi$.

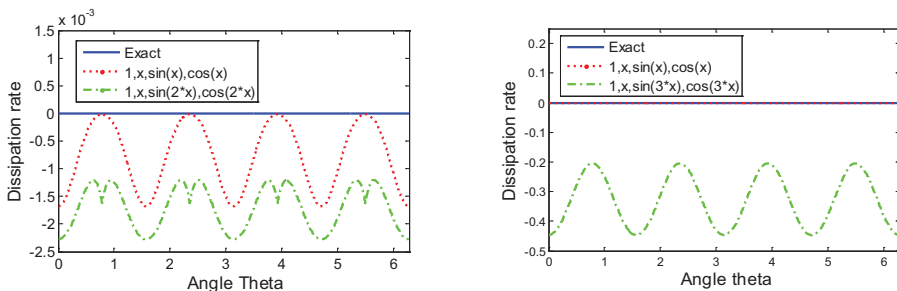


Figure 14: Dissipation rate ($\mathcal{R}^{\text{Im}}/K$) as function of $\theta (= \psi)$ for $Z = \pi$.

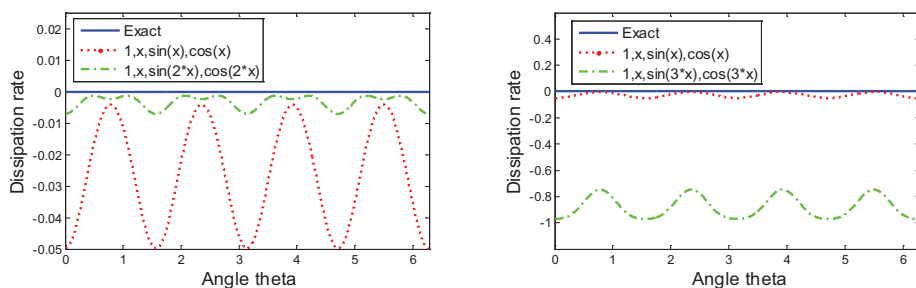


Figure 15: Dissipation rate ($\mathcal{R}^{\text{Im}}/K$) as function of $\theta (= \psi)$ for $Z = 1.5 * \pi$.

shown that the error of $(1, x, \sin(2*x), \cos(2*x)) < \text{the error of } (1, x, \sin(x), \cos(x)) < \text{the error of } (1, x, \sin(3*x), \cos(3*x))$.

The analysis shows that the accuracy of different schemes depends on various factors, including the wave number, wave direction and the solution basis. Figs. 12-15 indicate that both the dispersion and dissipation errors are the largest when $\theta = 0$ or $\theta = \pi/2$, which can be verified by the dispersion relation Eq. (4.5). The dispersion relation in the directions $\theta = 0$ or $\theta = \pi/2$ is identical to the corresponding one-dimensional analysis.

5 Numerical tests

5.1 One-dimensional numerical tests – A benchmark problem (CAA workshop, 2004)

A benchmark problem is solved here to verify some properties of the hybrid bases. The 1D convective wave equation with a unit wave speed is considered

$$\frac{\partial u}{\partial t} + \frac{\partial u}{\partial x} = 0. \quad (5.1)$$

The initial condition is given as

$$u(x, 0) = [2 + \cos(\beta*x)] \exp[-\ln 2(x/10)^2]. \quad (5.2)$$

Two different frequencies $\beta = 1.7$ and $\beta = 4.6$ are considered, and the mesh is set such that there is 1 DOF for each unit length. At this grid resolution, the high frequency wave embedded in the initial condition only has about 3.7 and 1.9 points-per-wave (PPW). It is therefore a challenge for any numerical scheme to adequately resolve the high frequency wave.

The hybrid bases which can resolve broadband waves are tested for this problem. In the first test, we employ a hybrid basis of the form $(1, x, \sin(\alpha*x), \cos(\alpha*x))$, with α chosen to resolve the initial high frequency wave $\cos(\beta*x)$ exactly. Since each element has 4 DOFs, we set $\Delta x = 3$. In the case of $\beta = 1.7$, $\alpha = 2.55$ allows the hybrid basis to exactly resolve $\cos(\beta*x)$. The time integration was carried out using a fourth-order four stage Runge-Kutta scheme. A constant time step 0.05 was used for all cases.

In Fig. 16, the numerical results of using base $(1, x, x^2, x^3)$, $(1, x, \sin(2.55*x), \cos(2.55*x))$ and $(1, x, \sin(4.0*x), \cos(4.0*x))$ are presented. It is obvious that $\alpha = 2.55$ produced the best results, which is as expected.

In Fig. 17, the solutions of the FOCPR schemes with 6 DOFs per element are presented. The mesh size is $\Delta x = 5$. The hybrid bases are in the form of $(1, x, x^2, x^3, \sin(4.0*x), \cos(4.0*x))$, $(1, x, \sin(3.0*x), \cos(3.0*x), \sin(4.5*x), \cos(4.5*x))$. The results are compared with that of the 6th order CPR scheme for both $\beta = 1.7$ and 4.6 at time = 500s. Both hybrid bases show much better resolution than the polynomial basis. It is clear that the more Fourier components there are in the basis, the more accurate the results are.

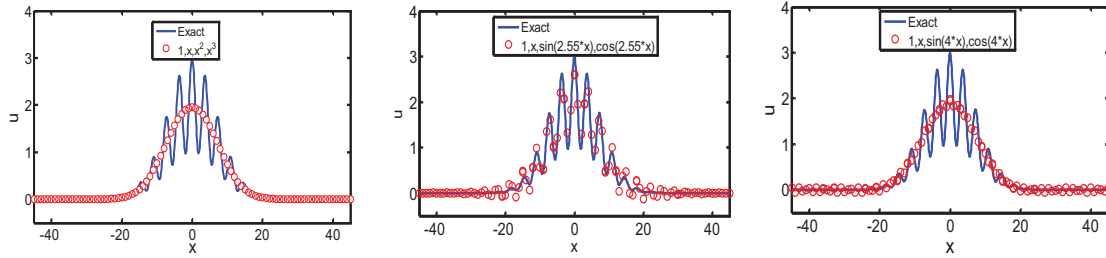


Figure 16: Numerical solution of 1D wave equation with the initial condition (5.6) for $\beta = 1.7$ ($T = 450s$ and $\Delta x = 3$, FOCPR schemes).

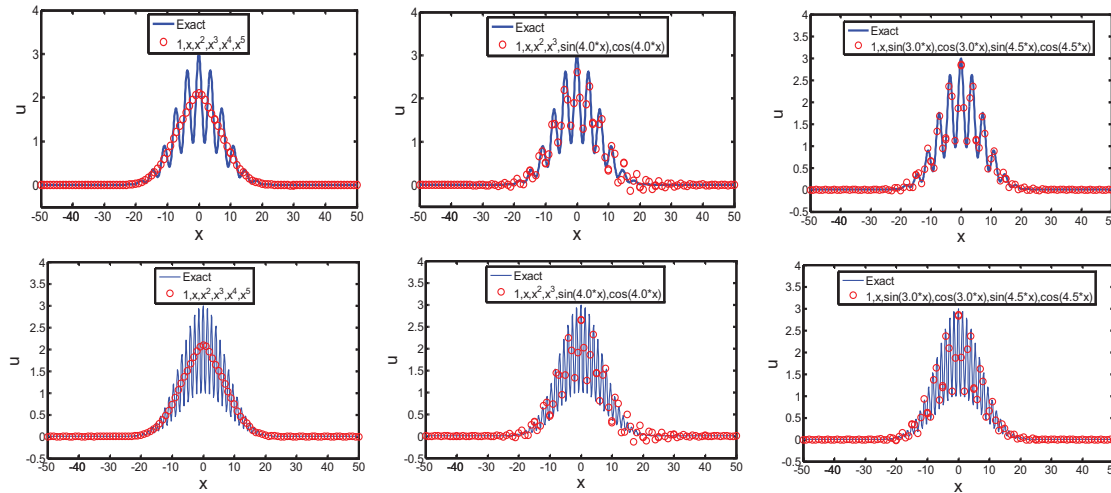


Figure 17: Numerical solution of 1D wave equation with the initial condition (5.6) ($T = 500s$ and $\Delta x = 5$, 6 DOF upwind) and first row $\beta = 1.7$ and second row $\beta = 4.6$.

5.2 Two-dimensional acoustic wave propagation

The propagation of acoustic waves generated by an acoustic pulse is simulated in 2D. The acoustic perturbations have small amplitude compared to the ambient flow variables. The exact solution for these problems can be used a reference. The governing equations are the 2D non-linear Euler equations

$$\frac{\partial Q}{\partial t} + \frac{\partial E}{\partial x} + \frac{\partial F}{\partial y} = 0, \tag{5.3}$$

where Q, E and F are vectors given by

$$Q = \begin{Bmatrix} \rho \\ \rho u \\ \rho v \\ E_t \end{Bmatrix}, \quad E = \begin{Bmatrix} \rho u \\ \rho u^2 + p \\ \rho uv \\ u(E_t + p) \end{Bmatrix}, \quad F = \begin{Bmatrix} \rho v \\ \rho uv \\ \rho v^2 + p \\ v(E_t + p) \end{Bmatrix}, \tag{5.4}$$

with ρ the mass density, u and v the velocity components in x and y directions and p the pressure. The total energy E_t is defined by the following equation

$$E_t = \frac{p}{\gamma - 1} + \rho \frac{u^2 + v^2}{2}, \tag{5.5}$$

where γ is set to 1.4 which is the ratio of specific heat to air. The initial solution is an acoustic pulse with a Gaussian profile and is set the same as one by Kris [38, 39]

$$\rho = \rho_\infty \left(1 + 0.001 * \exp \left(- \frac{(x - 0.5)^2 + (y - 0.5)^2}{\gamma_0^2} \right) \right), \tag{5.6a}$$

$$P = P_\infty + c_\infty^2 (\rho - \rho_\infty), \quad u = 0, \quad v = 0. \tag{5.6b}$$

And the ambient pressure, mass density and the half-width of the Gaussian profile are given as follow

$$P_\infty = 1, \quad \rho_\infty = 1, \quad r_0 = 0.05. \tag{5.7}$$

The exact solution of the linear Euler equations for the acoustic pressure field is given as

$$P_{ac}(t, x, y) = P - P_\infty = 0.001 * \frac{c_\infty^2 b^2}{2} \int_0^{+\infty} \exp \left(- \left(\frac{\xi b}{2} \right)^2 \right) \cos(\xi c_\infty t) J_0(\xi t) \xi d\xi, \tag{5.8}$$

with $\eta = \sqrt{(x - 0.5)^2 + (y - 0.5)^2}$ and J_0 is the zero-th order Bessel function of the first kind which is used as a reference solution [38, 39], b is the half width of the Gaussian profile and is set as 0.05.

The domain under considerations is a square $[0,1] \times [0,1]$. This domain is discretized by a uniform Cartesian grid. The computations are carried out on three different grids (5×5), (10×10) and (20×20). Roe's flux splitting is used as approximate Riemann solver. Time marching was done with a fourth-order, four stage Runge-Kutta scheme. All numerical simulations are carried out with $\Delta t = 0.0001s$ until $T = 0.3s$ and Gauss-Lobatto points are used as the solution points in each direction. The 10×10 grid is shown in Fig. 18(a) and the pressure contours are displayed in Fig. 18(b). The wave has not yet reached the boundary of the computational domain at $T = 0.3s$ and thus the far field boundary condition has negligible influence on the solution.

The profiles of the acoustic pressure at $y = 0.5$ computed with various CPR schemes are compared with the exact solution to assess the simulation accuracy. We focus on comparing the performance of various hybrid bases including the optimized ones.

First, we present results with 4 DOFs per element in each coordinate direction, i.e., 16 DOFs for the tensor product basis in 2D. In Fig. 19, the computational results with different basis on the 10×10 grid are displayed. It is obvious that the best result is obtained using the optimized basis $(1, x, \sin(2 * x), \cos(2 * x))$, which agrees with the previous analysis. On the finer 20×20 mesh, the computational results with various CPR schemes are compared in Fig. 20. Again, the best result is obtained with the optimized coefficient.

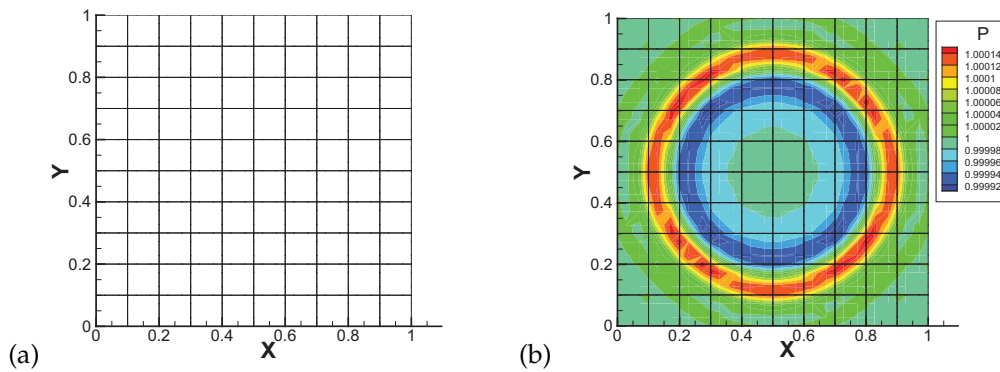


Figure 18: 10×10 Computational grid (a) and pressure contours (b) computed with the 4th order CPR scheme with a polynomial basis.

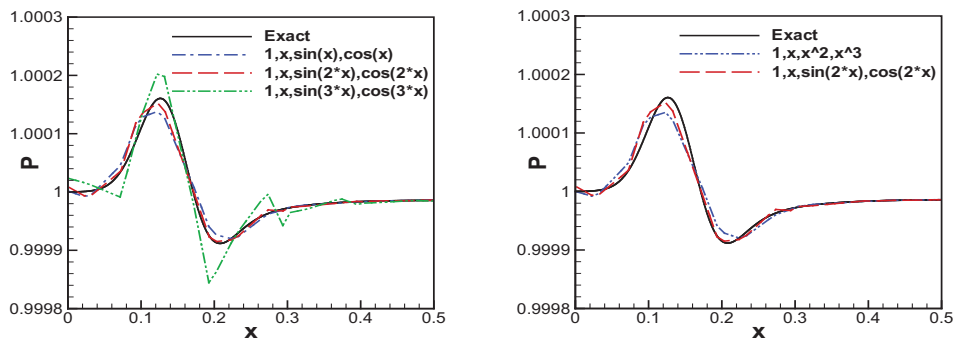


Figure 19: Pressure distribution at $y=0.5$ on 10×10 grids with $\Delta t=0.0001s$, $T=0.3S$ for 4 DOFs.

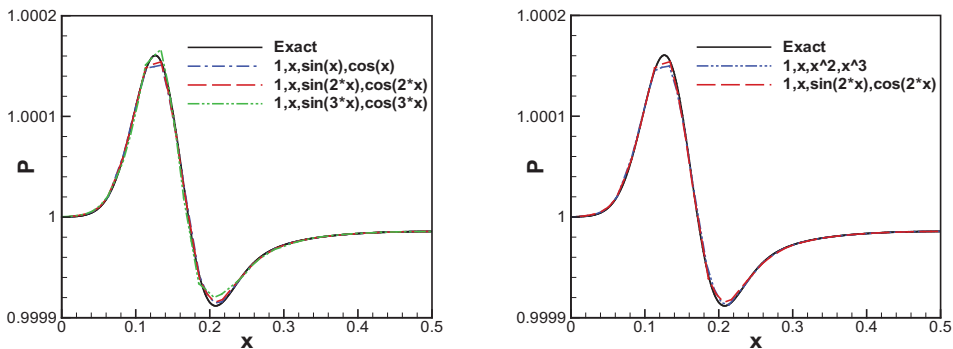


Figure 20: Pressure distribution at $y=0.5$ on 20×20 grids with $\Delta t=0.0001s$, $T=0.3S$ for 4 DOFs.

Obviously, when the mesh is finer, the difference between the computational results with different schemes becomes smaller. When the mesh is fine enough, the polynomial basis will perform the best as it has the highest nominal order of accuracy.

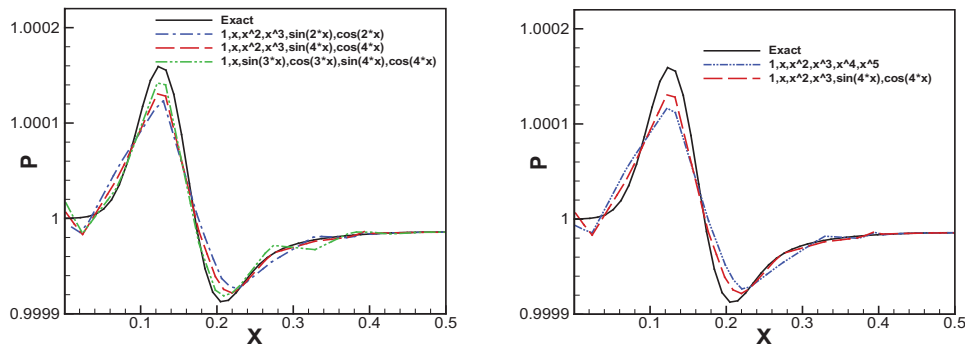


Figure 21: Pressure distribution along $y = 0.5$ on 5×5 grids at $T = 0.3s$ with 6 DOFs in each direction per element.

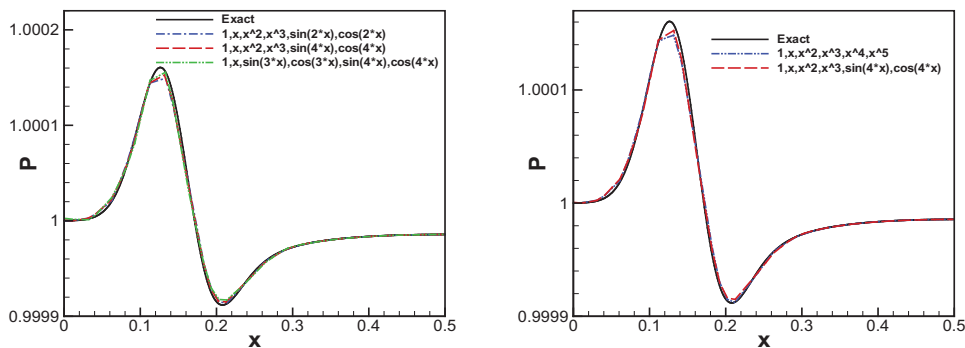


Figure 22: Pressure distribution along $y = 0.5$ on 10×10 grids at $T = 0.3s$ with 6 DOFs in each direction per element.

Next, we show results with 6 DOFs in each coordinate direction, or 36 DOFs per element. The simulations were performed on the two coarse meshes, 5×5 and 10×10 . Fig. 21 displays the results on the coarse mesh, while Fig. 22 shows the results on the fine mesh with various bases. It is clear that the best results were obtained by the FOCPR scheme with 2 Fourier components in the basis, i.e., $(1, x, \sin(3.0 * x), \cos(3.0 * x), \sin(4.0 * x), \cos(4.0 * x))$, followed by the FOCPR scheme with 1 Fourier component in the basis $(1, x, x^2, x^3, \sin(4.0 * x), \cos(4.0 * x))$. These results agree well with our previous analysis. It is obvious that the more Fourier components there are, the more accurate the results are.

6 Conclusions

In order to improve the resolution of the CPR formulation for broadband waves, Fourier components are introduced into the solution basis. Therefore, the solution basis includes both polynomials and cosine and sine functions. By optimizing the frequencies of the Fourier components, we obtain the frequency-optimized CPR method, which have small

dispersion and dissipation errors over a wide range of wave numbers. Comparisons are also made with the central and upwind DRP schemes, and the FOCPR schemes appear to have smaller dispersion or dissipation errors with similar cost. It is shown that more Fourier components in the basis result in smaller overall dispersion and dissipation errors. A mesh resolution analysis is also carried out to verify the optimization procedure. In the two-dimensional analysis, the tensor product bases are employed for quadrilateral grids. The accuracy of the FOCPR schemes strongly depends on the wave number, wave direction and the form of the basis.

Several numerical tests are conducted to verify the wave propagation analysis. The FOCPR formulation was tested with several benchmark problems from the 4th Computational Aeroacoustics (CAA) workshop. All the numerical results agree well with the error and the mesh resolution analysis. The FOCPR schemes perform better than the original CPR schemes for broadband waves, especial for high-frequency ones.

Appendix A

For the one-dimensional Eq. (3.9), the upwind Riemann flux formulation is used. Let the weighting functions be $\{W_l(\xi)|l=1,2,\dots,k+1\}$, where $k+1$ is the DOFs in each element, and ξ is the local coordinate $\xi \in [-1,1]$. The matrices in Eq. (3.9) are formed as

$$N_{mj}^{-1} = -2 * G^{-1} * W_m(-1) W_j(1), \quad m, j = 1, \dots, k+1, \quad (\text{A.1})$$

$$N_{mj}^0 = 2 * \frac{\partial W_j(\xi_m)}{\partial \xi} + 2 * G^{-1} * W_m(-1) W_j(-1), \quad m, j = 1, \dots, k+1, \quad (\text{A.2})$$

where G^{-1} is the inversion matrix of G , and $G_{m,j} = \int_{-1}^1 W_m(\xi) W_j(\xi) d\xi$, ($m, j = 1, \dots, k+1$).

For the two-dimensional Eq. (4.1), the upwind Riemann flux formulation is also used. The matrices in Eq. (4.4) are given as follows

$$N_{i,j}^{-1} = a_x \begin{cases} 0, & \text{if } f1(i-1, k+1) \neq f1(j-1, k+1), \\ -2 * G^{-1} * W_{f2(i, k+1)}(-1) W_{f2(j, k+1)}(1), & \text{if } f1(i-1, k+1) = f1(j-1, k+1), \end{cases} \quad (\text{A.3})$$

$$N_{i,j}^0 = a_x \begin{cases} 0, & \text{if } f1(i-1, k+1) \neq f1(j-1, k+1), \\ 2 * \frac{\partial W_j(\xi_{f2(i, k+1)})}{\partial \xi} - 2 * G^{-1} * W_{f2(i, k+1)}(-1) W_{f2(j, k+1)}(-1), & \text{if } f1(i-1, k+1) = f1(j-1, k+1), \end{cases} \quad (\text{A.4})$$

$$M_{i,j}^{-1} = a_y \begin{cases} 0, & \text{if } f2(i-1, k+1) \neq f2(j-1, k+1), \\ -2 * G^{-1} * W_{f1(i, k+1)}(-1) W_{f1(j, k+1)}(1), & \text{if } f2(i-1, k+1) = f2(j-1, k+1), \end{cases} \quad (\text{A.5})$$

$$M_{i,j}^0 = a_y \begin{cases} 0, & \text{if } f2(i-1,k+1) \neq f2(j-1,k+1), \\ 2 * \frac{\partial W_j(\xi_{f1(i,k+1)})}{\partial \xi} - 2 * G^{-1} * W_{f1(i,k+1)}(-1) W_{f1(j,k+1)}(-1), & \text{if } f2(i-1,k+1) = f2(j-1,k+1), \end{cases} \quad (\text{A.6})$$

where $f1$ denotes the rounded function, which is defined as $\text{floor}(i-1,k+1)$ in Matlab, and $f2$ is given as

$$f2(i,k+1) = \begin{cases} \text{mod}(i,k+1), & \text{if } \text{mod}(i,k+1) \neq 0, \\ k+1, & \text{if } \text{mod}(i,k+1) = 0, \end{cases} \quad (\text{A.7})$$

where mod is defined as the complement function, such as the mod function in Matlab.

Acknowledgments

This study has been supported by the Department of Aerospace Engineering in Iowa State University and partially supported by the Air Force office of Scientific Research.

References

- [1] R. Abgrall, P.L. Roe, High order fluctuation schemes on triangular meshes, J. Sci. Comput. 19 (2003) 3-36.
- [2] G. Ashcroft, X. Zhang, Optimized prefactored compact schemes, J. Comput. Phys. 190 (2003) 459-477.
- [3] D. Balsara, C.-W. Shu, Monotonicity preserving weighted essentially non-oscillatory schemes with increasing high order of accuracy, J. Comput. Phys. 160 (2000) 405-452.
- [4] T.J. Barth, P.O. Frederickso, High-order solution of the Euler equations on unstructured grids using quadratic reconstruction, AIAA Paper 96-0027, 1996.
- [5] F. Bassi, S. Rebay, High-order accurate discontinuous finite element solution of the 2D euler equations, J. Comput. Phys. 138 (1997) 251-285.
- [6] S. Christofi, The study of building blocks for essentially non-oscillatory (ENO) schemes, Ph.D. thesis, Division of Applied Mathematics, Brown University, 1996.
- [7] B. Cockburn, F. Li, C.-W. Shu, Locally divergence-free discontinuous Galerkin methods for the Maxwell equations, J. Comput. Phys. 194 (2004) 588-610.
- [8] B. Cockburn, C.-W. Shu, TVB Runge-Kutta local projection discontinuous Galerkin finite element method for conservation laws II: General framework, Math. Comput. 52 (1989) 411-435.
- [9] B. Cockburn, C.-W. Shu, The Runge-Kutta discontinuous Galerkin method for conservation laws V: Multidimensional systems, J. Comput. Phys. 141 (1998) 199-224.
- [10] B. Costa, W.-S. Don, Multi-domain hybrid spectral-WENO methods for hyperbolic conservation laws, J. Comput. Phys. 224 (2007) 970-991.
- [11] J.A. Ekaterinaris, High-order accurate, low numerical diffusion methods for aerodynamics, Prog. Aerosp. Sci. 41 (2005) 192-300.
- [12] H. Gao, Z.J. Wang, A conservative correction procedures via reconstruction formulation with the Chain-rule divergence evaluation, submitted.
- [13] R. Hixon, A new class of compact schemes, AIAA paper 98-0367, 1998.

- [14] C.-Q. Hu, C.-W. Shu, Weighted essentially Non-oscillatory schemes on Triangular meshes, *J. Comput. Phys.* 150 (1999) 97-127.
- [15] F.-Q. Hu, M.Y. Hussaini, P. Rasetarinera, An analysis of the discontinuous Galerkin method for wave propagation problems, *J. Comput. Phys.* 151 (1999) 921-946.
- [16] P.G. Huang, Z.J. Wang, Y. Liu, An implicit space-time spectral difference method for discontinuity capturing using adaptive polynomials, *AIAA Paper* 2005-5255, 2005.
- [17] H.T. Huynh, A flux reconstruction approach to high-order schemes including discontinuous Galerkin methods, *AIAA paper* 2007-4079, 2007.
- [18] H.-M. Jurgens, High-accuracy finite-difference schemes for linear wave propagation, Ph.D thesis, Department of Aerospace Science and Engineering, University of Toronto, 1997.
- [19] M.K. Kadalbajoo, K.C. Patidar, Exponentially fitted spline in compression for the numerical solution of singular perturbation problems, *Comput. Math. Appl.* 46 (2003) 751-767.
- [20] D.-A. Kopriva, J.-H. Kolas, A conservative staggered-grid Chebyshev multidomain method for compressible flows, *J. Comput. Phys.* 125 (1996) 244-261.
- [21] D.-A. Kopriva, A staggered-grid multidomain spectral method for compressible Navier-Stokes equations, *J. Comput. Phys.* 143 (1998) 125-158.
- [22] F. Li, C.-W. Shu, Locally divergence-free discontinuous Galerkin methods for MHD equations, *J. Sci. Comput.* 22-23 (2005) 413-442.
- [23] F. Li, C.-W. Shu, Reinterpretation and simplified implementation of a discontinuous Galerkin method for Hamilton-Jacobi equations, *Appl. Math. Lett.* 18 (2005) 1204-1209.
- [24] F. Li, C.-W. Shu, A local-structure-preserving local discontinuous Galerkin method for the Laplace equation, *Meth. Appl. Anal.* 13 (2006) 215-234.
- [25] Y.-G. Li, Wavenumber-extended high-order upwind-biased finite-difference schemes for convective scalar transport, *J. Comput. Phys.* 133 (1997) 235-255.
- [26] Y. Liu, M. Vinokur, Z.J. Wang, Discontinuous spectral difference methods for conservation laws on unstructured grids, in C. Groth and D.W. Zingg (Eds.), *Proceeding of the 3rd international conference in CFD, Toronto, Springer, 2004*, pp. 449-454.
- [27] Y. Liu, M. Vinokur, Z.J. Wang, Spectral (finite) volume method for conservation laws on unstructured grids V: Extension to three-dimensional systems, *J. Comput. Phys.* 212 (2006) 454-472.
- [28] Y. Liu, M. Vinokur, Z.J. Wang, Spectral difference methods for unstructured grids I. Basic formulation, *J. Comput Phys.* 216 (2006) 780-801.
- [29] G. May, A. Jameson, A spectral difference method for the Euler and Navier-Stokes equations on unstructured grids, *AIAA Paper* 2006-304, 2006.
- [30] A.T. Patera, A spectral element method for fluid dynamics: Laminar flow in a channel expansion, *J. Comput. Phys.* 54 (1984) 468-488.
- [31] Y.N. Reddy, P.P. Chakravarthy, An exponentially fitted finite difference method for singular perturbation problems, *Appl. Math. Comput.* 154 (2004) 83.
- [32] H.-Q. Sia, T.-G. Wang, Grid-optimized upwind dispersion-relation-preserving scheme on non-uniform Cartesian grids for computational aeroacoustics, *Aerosp. Sci. Tech.* 12 (2008) 608-617.
- [33] Y. Sun, Z.J. Wang, Y. Liu, Spectral (finite) volume method for conservation laws on unstructured grids VI: Extension to viscous flow, *J. Comput. Phys.* 215 (2006) 41-58.
- [34] Y. Sun, Z.J. Wang, Y. Liu, High-order multidomain spectral difference method for the Navier-Stokes equations on unstructured hexahedral grids, *Commun. Comput. Phys.* 2(2) (2007) 310-333.
- [35] Y. Sun, Z.J. Wang, Y. Liu, C.L. Chen, Efficient implicit LU-SGS algorithm for high-order

- spectral difference method on unstructured hexahedral grids, AIAA Paper, 2007-0313, 2007.
- [36] C.K.W. Tam, Computational aeroacoustics: Issues and methods, AIAA J., 33(10) (1995) 1788-1796.
 - [37] C.K.W. Tam, J.-C. Webb, Dispersion-relation-preserving finite difference schemes for computational acoustics, J. Comput. Phys. 107 (1993) 262-281.
 - [38] K. Van den Abeele, Development of high-order accurate schemes for unstructured grids, Ph.D thesis, Department of Mechanical Engineering, Vrije Universiteit Brussel, Belgium, 2008.
 - [39] K. Van den Abeele, C. Lacor, An accuracy and stability study of the 2D spectral volume method, J. Comput. Phys. 226 (2007) 1007-1026.
 - [40] K. Van den Abeele, C. Lacor, Z.J. Wang, On the connection between the spectral volume and the spectral difference method, J. Comput. Phys. 227 (2007) 877-885.
 - [41] K. Van den Abeele, C. Lacor, Z.J. Wang, On the stability and the accuracy of the spectral difference method, J. Sci. Comput. 37(2) (2008) 162-188.
 - [42] K. Van den Abeele, T. Broeckhoven, C. Lacor, Dispersion and dissipation properties of the 1D spectral volume method and application to a p-multigrid algorithm, J. Comput. Phys. 224 (2007) 616-636.
 - [43] Z.J. Wang, Spectral (finite) volume method for conservation laws on unstructured grids: basic formulation, J. Comput. Phys. 178 (2002) 210-251.
 - [44] Z.J. Wang, High-order methods for the Euler and Navier-Stokes equations on unstructured grids, J. Prog. Aerosp. Sci. 43 (2007) 1-41.
 - [45] Z.J. Wang, R.F. Chen, Optimized weighted essentially nonoscillatory schemes for linear waves with discontinuity, J. Comput. Phys. 174 (2001) 381-404.
 - [46] Z.J. Wang, H.-Y Gao, A unifying lifting collocation penalty formulation including the discontinuous Galerkin, spectral volume/difference methods for conservation laws on mixed grids, J. Comput. Phys. 228 (2009) 8161-8186.
 - [47] Z.J. Wang, Y. Liu, Spectral (finite) volume method for conservation laws on unstructured grids II: Extension to two-dimensional scalar equation, J. Comput. Phys. 179 (2002) 665-697.
 - [48] Z.J. Wang, Y. Liu, Spectral (finite) volume method for conservation laws on unstructured grids III: Extension to one-dimensional systems, J. Sci. Comput. 20 (2004) 137-157.
 - [49] Z.J. Wang, L. Zhang, Y. Liu, Spectral (finite) volume method for conservation laws on unstructured grids III: Extension to two-dimensional systems, J. Sci. Comput. 194 (2004) 716-741.
 - [50] Z.J. Wang, Y. Liu, The spectral difference method for the 2D Euler equations on unstructured grids, AIAA Paper 2005-5112, 2005.
 - [51] Z.J. Wang, Y. Liu, G. May, A. Jameson, Spectral difference method for unstructured grids II: Extension to the Euler equations, J. Sci. Comput. 32(1) (2007) 45-71.
 - [52] L. Yuan, C.-W. Shu, Discontinuous Galerkin method based on non-polynomial approximation spaces, J. Comput. Phys. 218 (2006) 295-323.
 - [53] D.W. Zingg, A review of high-order and optimized finite difference methods for simulating linear wave phenomena, AIAA Paper 97-2088, 1997.
 - [54] M. Zhuang, R.F. Chen, Optimized upwind dispersion-relation-preserving finite difference scheme for computational aeroacoustics, AIAA J. 36(11) (1998) 2146-2148.
 - [55] M. Zhuang, R.F. Chen, Application of high-order optimized upwind schemes for computational aeroacoustics, AIAA J. 40(3) (2002) 443-449.